Journal of Materials Chemistry C

ROYAL SOCIETY OF CHEMISTRY

PAPER

View Article Online
View Journal | View Issue

Published on 04 February 2020. Downloaded by Lomonosov Moscow State University on 3/19/2020 4:47:56 PM.

Check for updates

Cite this: J. Mater. Chem. C, 2020, 8, 3509

Materials synthesis, characterization and DFT calculations of the visible-light-active perovskite-like barium bismuthate $Ba_{1.264(4)}Bi_{1.971(4)}O_4$ photocatalyst†

D. S. Shtarev, [ab] A. V. Shtareva, [ab] R. Kevorkyants, [c] A. V. Rudakova, [c] M. S. Molokeev, [bde] T. V. Bakiev, [c] K. M. Bulanin, [cf] V. K. Ryabchuk [cf] and N. Serpone *[g]

Received 25th November 2019,
Accepted 3rd February 2020

DOI: 10.1039/c9tc06457e

rsc.li/materials-c

A perovskite-like barium bismuthate of the $BaBi_2O_4$ class, $Ba_{1.264(4)}Bi_{1.971(4)}O_4$, has been prepared by solid-state synthesis and subsequently characterized by a number of experimental techniques (XPS, DRS, SEM, EDX and Raman spectroscopy), as well as by a DFT computational approach using the GGA Perdew–Burke–Ernzerhof (PBE) density functional to determine the energy band structure. XRD peaks were indexed to a rhombohedral cell ($R\bar{3}m$) with parameters close to $Ba_{0.156}Bi_{0.844}O_{1.422}$ (*i.e.*, to $Ba_{0.439}Bi_{2.374}O_4$), which upon Rietveld refinement gave $Ba_{1.264(4)}Bi_{1.971(4)}O_4$. The Bi–O bond lengths determined from this refinement (1.86 and 2.31 Å) accorded with the bond lengths estimated from Raman spectra (1.97 and 2.26 Å). DFT calculations revealed the bismuthate to display two bandgaps that correspond to lower-energy indirect (2.28 eV) and to higher-energy direct (2.36 eV) electronic transitions in good agreement with the experimental bandgaps of 2.26 eV and 2.43 eV, respectively, from Tauc plots of DRS spectra. Relative to the indirect bandgap energy of 2.26 eV, the energies of the valence band and of the conduction band were, respectively, +1.14 eV and −1.12 eV. The photoactivity of $Ba_{1.264(4)}Bi_{1.971(4)}O_4$ was examined toward the photoreduction of the greenhouse gas CO_2 in aqueous media photoelectrochemically yielding alcohols and alkanes, while in the gas phase in an infrared cell reactor the products were carbon monoxide and alkanes.

1. Introduction

The search for novel visible-light-active (VLA) semiconductor photocatalysts has been an active field of investigation for several decades.[1–4] Such materials have typically found applications in a number of significant areas: (i) purification of water and air contaminated with organic/inorganic pollutants (ecology), (ii) photocatalytic decomposition of water (more precisely, water splitting to produce a solar fuel; energy), and (iii) environmental reduction of the greenhouse gas CO_2 to produce a solar fuel such as CH_4 and/or CH_3OH among others (ecology and energy).

Within the present context, a number of experimental[5] and theoretical[6,7] studies have reported an anomalous ratio in a series of alkaline-earth bismuthates between the bandgap width and the energy of the conduction band. In particular, bismuthates of heavy alkaline-earth metals (*e.g.*, those of Sr and Ba) are expected to demonstrate the lowest potentials of the conduction band together with reasonable bandgap energies. In this regard, the photocatalytic properties of some basic strontium bismuthates have been reported.[5,8–13] Of these, only the barium bismuthate double perovskite $Ba_2Bi^{3+}Bi^{5+}O_6$

[a] Yu. A. Kosygin Institute of Tectonics and Geophysics, Far Eastern branch of the Russian Academy of Sciences, 65 Kim Yu Chen Street, Khabarovsk, 680063, Russian Federation. E-mail: shtarev@mail.ru, avshtareva@mail.ru
[b] Far Eastern State Transport University, 47 Seryshev Street, Khabarovsk, 680021, Russian Federation. E-mail: msmolokeev@mail.ru
[c] Saint-Petersburg State University, Laboratory "Photoactive Nanocomposite Materials", Ul'yanovskaya 1, Petergof, Saint-Petersburg, 198904, Russian Federation. E-mail: ruslan.kevorkyants@gmail.com, aida.rudakova@spbu.ru, tairbakiev@gmail.com, v.ryabchuk@spbu.ru, k.bulanin@spbu.ru
[d] Kirensky Institute of Physics, Akademgorodok 50, bld. 38, Krasnoyarsk, 660036, Russian Federation. E-mail: msmolokeev@mail.ru
[e] Siberian Federal University, 79 Svobodny pr., 660041 Krasnoyarsk, Russian Federation. E-mail: msmolokeev@mail.ru
[f] Saint-Petersburg State University, Department of Photonics, Ul'yanovskaya 1, Petergof, Saint-Petersburg, 198904, Russian Federation
[g] PhotoGreen Laboratory, Dipartimento di Chimica, Universita di Pavia, via Taramelli 12, Pavia 27100, Italy. E-mail: nick.serpone@unipv.it

† Electronic supplementary information (ESI) available: Scheme of the PEC cell system, chromatograms of the photoreduction of CO_2, EDX spectral results and XPS spectra data together with FTIR evidence of CO_2 photoreduction products, and the time course of the (non)degradation of phenol. CCDC 1962724. For ESI and crystallographic data in CIF or other electronic format see DOI: 10.1039/c9tc06457e

Published on 04 February 2020. Downloaded by Lomonosov Moscow State University on 3/19/2020 4:47:56 PM.

(empirically, $BaBiO_3$) has been examined systematically in a number of photocatalytic studies.[14–18] For instance, Lee and coworkers[14] showed that this material is a p-type semiconductor, which has been shown to act as a photocatalyst in a number of reactions including photocatalytic water splitting.[15–18] However, determination of its bandgap has revealed a large discrepancy between theory and experiment; theory predicted a bandgap of 1.00–1.45 eV,[19–21] whereas experiments placed the bandgap substantially greater at 1.41–2.05 eV.[15–18,22,23] Presumably, this inconsistency is likely caused by the two oxidation states of bismuth present in the structure (*viz.*, Bi^{3+} and Bi^{5+}).

The critical intrinsic limitation on the use of novel semiconducting photocatalysts is their bandgap energy. Visible light photoactivation of such materials is possible only if their bandgaps do not exceed 3.3 eV (see *e.g.*, ref. 24 and references therein). Depending on the particular application, additional limitations could be imposed on the fundamental properties of such materials such as, for instance, the redox potentials of the valence band (E_{VB}) and the conduction band (E_{CB}).

While the photocatalytic water splitting process is an eco-friendly source of energy (H_2 as the fuel), reduction of CO_2 to other more useful substrates is, in addition to energy generation, a means to potentially reduce the controversial threat of global warming by diminishing the atmospheric concentration of this greenhouse gas. This is substantiated by the increasing number of publications associated with the photoreduction of CO_2 *vis-à-vis* a decreasing number of publications during the last two years with regard to the water splitting process.[4]

Occurrence of the photocatalytic water splitting process requires the redox potential of the conduction band to be negative because $E(H^+/H_2) = 0.00$ V (*versus* the NHE scale) and for the valence band to be >1.23 eV because $E(O_2/H_2O) = 1.23$ V at pH 7. By contrast, the photoreduction of CO_2 may take place when $E_{CB} < -0.24$ to -0.61 eV as the relevant redox potentials of its half-reactions are in this range. According to empirical models for a set of simple oxides,[25] the lowering of the conduction band level is accompanied by an increase of the bandgap width, which drastically limits the choice of materials suitable for practical photoreduction of CO_2.

Our current study reports (for the first time) a systematic theoretical and experimental study of another promising perovskite-like barium bismuthate of the $BaBi_2O_4$ class, with regard to its synthesis and characterization of the structure and electronic and optical properties, together with its visible-light-photoactivity toward the photoinduced reduction of the greenhouse gas carbon dioxide.

2. Results and discussion

2.1. Structure and composition of the as-synthesized barium bismuthate

The structure and the unit cell composition of the as-synthesized barium bismuthate were investigated by X-ray diffraction methods.

Fig. 1 displays the XRD pattern of the barium bismuthate and the results of the Rietveld analysis.

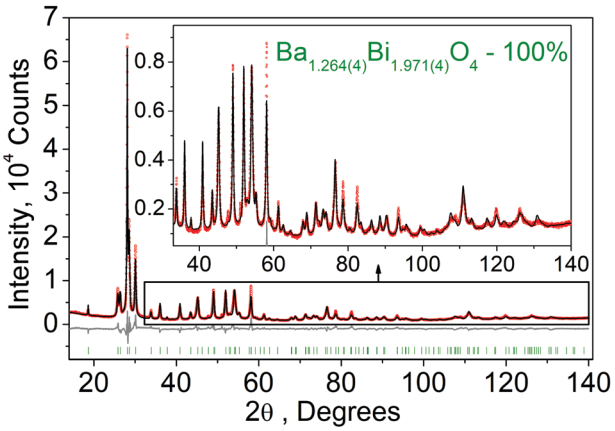

Fig. 1 Difference Rietveld plot of $Ba_{1.264(4)}Bi_{1.971(4)}O_4$. Red dots depict the experimental XRD powder pattern; the black solid line shows the pattern calculated from the structure; the grey solid line below refers to the difference between the experimental and calculated patterns; and the green vertical lines depict the Bragg peak positions. The inset shows an enlarged view of the plot and the chemical formula of the compound investigated.

All peaks were indexed to a rhombohedral cell ($R\bar{3}m$) with parameters that were close to $Ba_{0.156}Bi_{0.844}O_{1.422}$ (or, that is, to $Ba_{0.439}Bi_{2.374}O_4$).[26]

Consequently, this crystal structure was taken as the starting model for Rietveld refinement. The occupation values of all ions were refined with no restraints. The refinement was stable and gave low *R*-factors (Table 1 and Fig. 2). The coordinates of the atoms and main bond lengths are collected in Tables 2 and 3, respectively. The chemical formula obtained from the refinement could thus be written as $Ba_{1.264(4)}Bi_{1.971(4)}O_4$ (Fig. 1). The small sum of the charges (+0.44) implies that the number of oxygen vacancies in the structure is overestimated, which is often the case in such systems because of difficulties in refining the occupancy of light ions in the presence of heavy metal ions. Thus, it could be argued that a perovskite-like barium bismuthate of the $BaBi_2O_4$-type was successfully synthesized.[27]

Four main characteristic spectral ranges were identified in the Raman spectrum of the synthesized barium bismuthate sample (spectrum shown in Fig. 3): (1) the broad peak at 215–300 cm^{-1} is assigned to Ba–O vibrations,[28] (2) the noticeable high-frequency shoulder in the 300–330 cm^{-1} range is ascribed to Bi–O–Bi asymmetric stretch vibrations,[29] (3) the peak at

Table 1 Main parameters from the processing and refinement of the $Ba_{1.264(4)}Bi_{1.971(4)}O_4$ system

Compound	$Ba_{1.264(4)}Bi_{1.971(4)}O_4$
Space group	$R\bar{3}m$
a, Å	4.0069 (3)
c, Å	28.534 (2)
V, Å^3	396.74 (5)
2θ-interval, degrees	15–140
R_{wp}, %	8.07
R_p, %	5.99
R_{exp}, %	2.22
χ^2	3.64
R_B, %	3.39

 This journal is © The Royal Society of Chemistry 2020

Published on 04 February 2020. Downloaded by Lomonosov Moscow State University on 3/19/2020 4:47:56 PM.

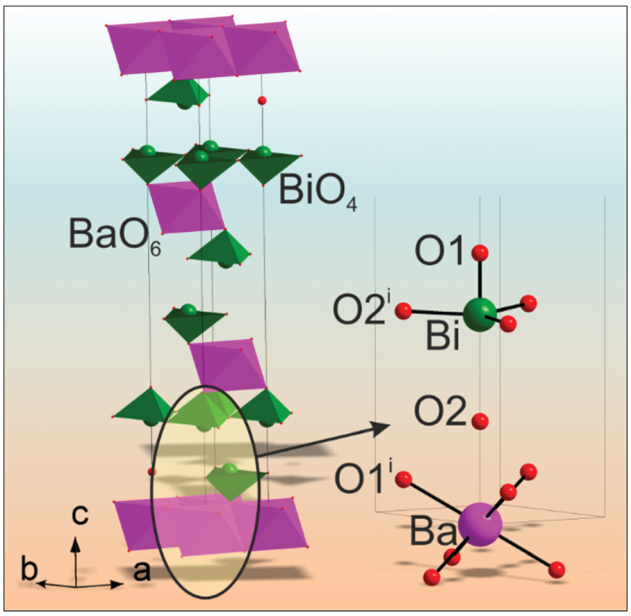

Fig. 2 The crystal structure of $Ba_{1.264(4)}Bi_{1.971(4)}O_4$. Purple octahedra denote the BaO_6 function; green trigonal pyramids refer to the BiO_4 functions with the green Bi atom inside; and red spheres denote the oxide ions. Ions with the "i" label depict symmetrically equivalent ions.

Table 2 Fractional atomic coordinates and isotropic displacement parameters (Å^2) of $BaBi_2O_4$

	x	y	z	B_{iso}	Occupancy
Ba	0	0	0	0.7 (2)	0.529 (2)
Bi	0	0	0.22227 (3)	0.3 (2)	0.4121 (8)
O(1)	0	0	0.2874 (3)	2.0 (5)	0.569 (5)
O(2)	0	0	0.109 (1)	2.0 (7)	0.268 (4)

Table 3 Main bond lengths (Å) of $BaBi_2O_4$ (symmetry codes: (i) $-x - 1/3$, $-x + y + 1/3$, $-z + 1/3$)

Ba(1)–O(1)^i	2.660 (5)
Bi(1)–O(1)	1.86 (1)
Bi(1)–O(2)^i	2.3140 (7)

515 cm^{-1} is due to Ba–O vibrations,[29] and (4) the most intense and narrow peak at 647 cm^{-1} corresponds to the Bi–O$^-$ stretching modes.[30,31]

Using the empirical expression (eqn (1)) found for bismuth oxides that relates the Bi–O bond lengths (R) to the Raman stretching frequencies in cm^{-1} (υ)[32] makes it possible to calculate the bond lengths for the Bi–O vibrations at 647 cm^{-1} and 315 cm^{-1} of the studied sample.

$$\upsilon = 92\,760e^{-2.511R} \quad (1)$$

The bond lengths thus estimated are 1.97 Å and 2.26 Å, respectively, which correspond to the lengths for the Bi(1)—O(1) and Bi(1)—O(2)^i bonds determined from the Rietveld refinement for the $Ba_{1.264(4)}Bi_{1.971(4)}O_4$ compound (Table 3 and Fig. 2).

Fig. 4 illustrates the scanning electron microscopy (SEM) images of the synthesized barium bismuthate particle. Evidently, the

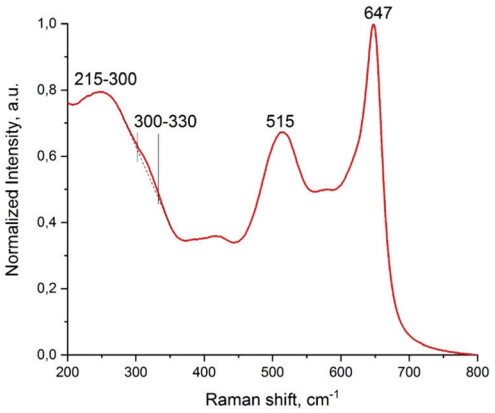

Fig. 3 Raman spectrum of the as-synthesized barium bismuthate, $Ba_{1.264(4)}Bi_{1.971(4)}O_4$, sample.

particles tend to be rather large (20 μm) and possess a poorly developed surface, albeit a layered structure. This is especially noticeable in Fig. 4b.

The particles are agglomerates of 'scales' that could be a result of the powder pressing during the sample preparation procedure (see the Synthesis and characterization section).

The specific surface area determined by the BET technique was *ca.* 0.5 m^2 g^{-1}, which corresponds to a practically non-porous

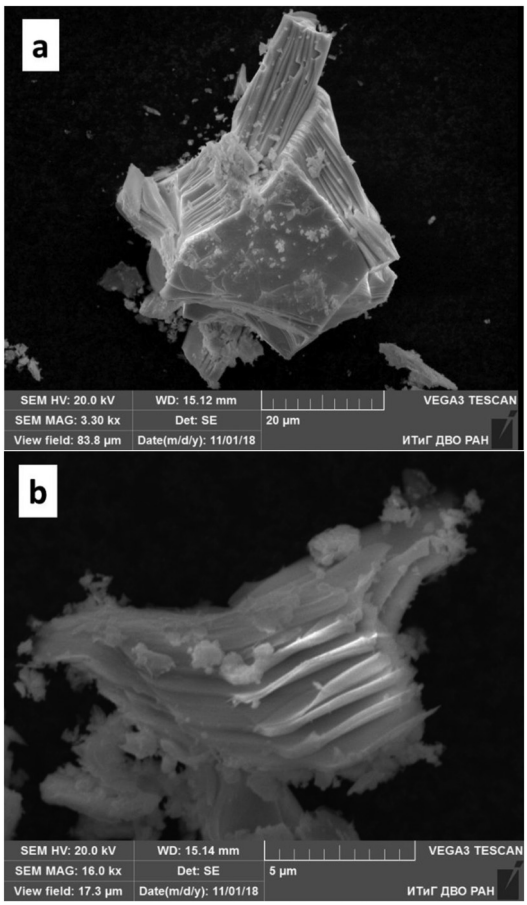

Fig. 4 SEM images of the barium bismuthate synthesized particles.

Published on 04 February 2020. Downloaded by Lomonosov Moscow State University on 3/19/2020 4:47:56 PM.

sample. Data on the surface morphology are consistent with the SEM micro-images.

EDX spectra of the as-synthesized barium bismuthate particles (reported in Fig. S1 in the ESI†) show that all chemical elements (Ba, Bi, and O) in the compound are regularly distributed over its volume. No impurity elements were observed.

The elemental composition of the sample's surface was analyzed using XPS techniques (spectra illustrated in Fig. S2, ESI†). The XPS data infer that barium and bismuth are present in single oxidation states, namely Ba^{2+} and Bi^{3+}. The oxygen line demonstrates a more complex structure and can be represented as a sum of four Gaussians (see Fig. S2c, ESI†). The two Gaussians at 531 eV and 532 eV are associated with the O–C═O bonds of chemisorbed carbon dioxide molecules. The presence of such chemisorbed species on the surface is characteristic of compounds containing alkaline earth metals. The other two lower-energy spectral lines correspond to oxygen in different oxidation states. The binding energy (BE) peak at 529.4 eV is due to the oxygen dianion O^{2-}, whereas the peak at 530.6 eV can be assigned to the oxide anion O^{-}, in agreement with that obtained from the Rietveld refinement of the chemical formula in that the $Ba_{1.264(4)}Bi_{1.971(4)}O_4$ compound is partially positively overcharged (+0.44) owing to the presence of oxygen vacancies. Apparently, the presence of anion vacancies is typical of alkaline earth metal bismuthates. In this regard, various oxygen vacancies in strontium bismuthates have been established by Shtarev and coworkers.[5]

2.2. Electronic band structure of the barium bismuthate

The electronic band structure includes the energy position of the edges of the conduction (CB) and valence (VB) bands with respect to the vacuum level. The positions of the conduction (E_{CB}) and valence (E_{VB}) bands, together with the bandgap energies (E_g), can be determined experimentally by measuring at least any two of these three values (*i.e.*, E_{CB} and E_g or E_{VB} and E_g). Note that knowledge of such an energy level diagram of the material under examination facilitates placing the electrochemical potentials of important redox reactions relative to the CB and VB.

For the barium bismuthate $BaBi_2O_4$, the valence band and the bandgap energies were measured experimentally by X-ray photoelectron spectroscopy (XPS) techniques and by Tauc plots, respectively. The top of the valence band for the $Ba_{1.264(4)}Bi_{1.971(4)}O_4$ sample was determined using the low-energy edge of the XPS spectrum in the O2p region (Fig. 5), which gave +1.14 eV (relative to NHE) as the energy position of the top of the valence band.[33]

The bandgap energy for the $Ba_{1.264(4)}Bi_{1.971(4)}O_4$ sample was determined using DRS methods. The absorption spectrum displayed in Fig. 6a clearly demonstrates that the material absorbs light well into the visible range. Moreover, the reflectance (>0.8) near the edge of the intrinsic absorption allows the use of the Kubelka–Munk transformation and the application of the Tauc method in determining the bandgap energy. Tauc plots for both direct (the value of the exponent is 2) and indirect (the value of the exponent is 1/2) yielded allowed electronic transitions as reported in Fig. 6b; extrapolation of the linear regions of the plots yielded 2.43 eV for the direct bandgap and 2.26 eV for the indirect bandgap.

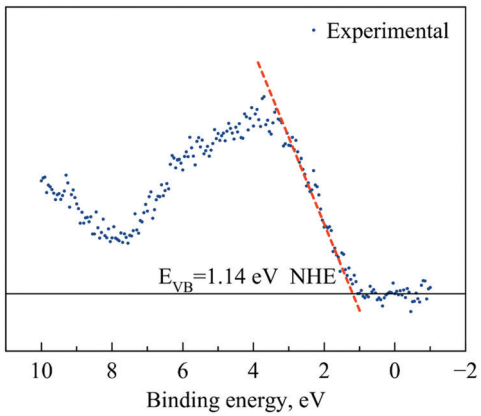

Fig. 5 XPS spectrum of the synthesized $Ba_{1.264(4)}Bi_{1.971(4)}O_4$ bismuthate sample in the O2p region. The horizontal black line is the XPS baseline, whereas the dashed red line is the linear extrapolation of the low-energy edge of the spectrum. The binding energy scale is presented relative to NHE in accordance with the methodology given in ref. 33.

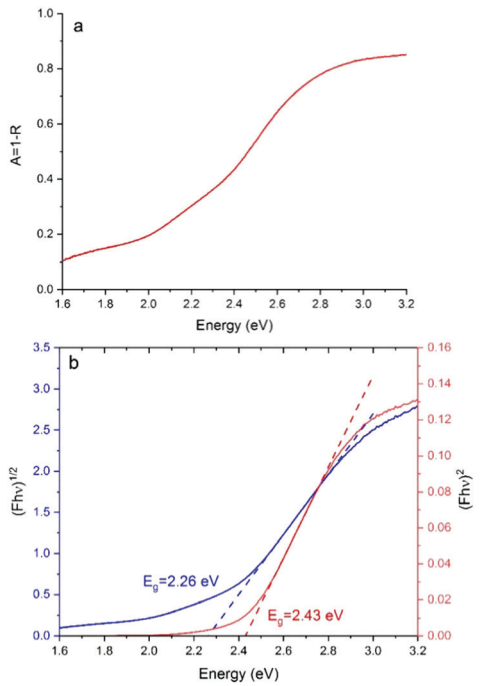

Fig. 6 (a) Diffuse reflectance spectra displayed as absorptance $A = (1 - R)$ spectra of the barium bismuthate sample. (b) Tauc plot assuming direct (red) and indirect (blue) electronic transitions.

In addition to spectroscopic studies, the electronic band structure of $Ba_{1.264(4)}Bi_{1.971(4)}O_4$ was also modeled using DFT calculations, the results of which are presented in Fig. 7 for the computed electronic band structure and the density of states. Results from these DFT calculations suggest that the bismuthate displays two bandgaps that correspond to lower-energy indirect (2.28 eV) and to higher-energy direct (2.36 eV) electronic transitions. A comparison of the experimental and

 This journal is © The Royal Society of Chemistry 2020

Published on 04 February 2020. Downloaded by Lomonosov Moscow State University on 3/19/2020 4:47:56 PM.

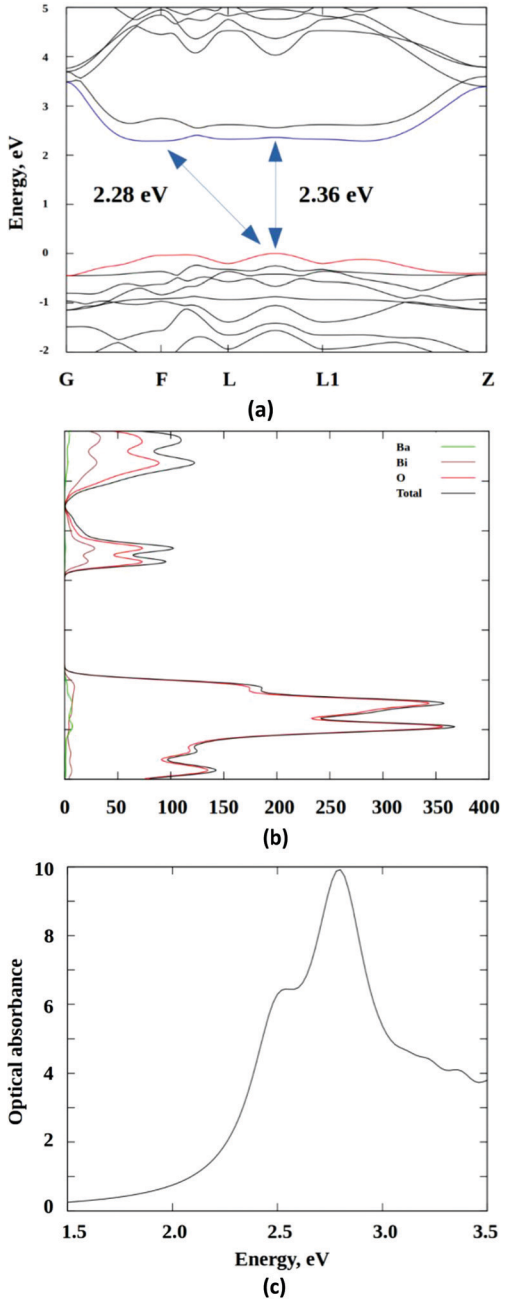

Fig. 7 Electronic band structure (a) and density of states (b), together with the computed optical absorption spectrum (c) of the barium bismuthate system.

theoretical bandgaps (compare Fig. 6b with Fig. 7a) reveals good agreement between the experimental (2.26 eV) and the computed (2.28 eV) indirect bandgap. The theoretically calculated direct bandgap of 2.36 eV is also in fairly good accord with its experimental counterpart (2.43 eV). To the extent that theoretical calculations predict indirect allowed transitions, we used the experimental bandgap of 2.26 eV to construct the band diagram of the $BaBi_2O_4$-type bismuthate.

The calculated density of states of the barium bismuthate indicates that the valence band is formed only by oxygen-related

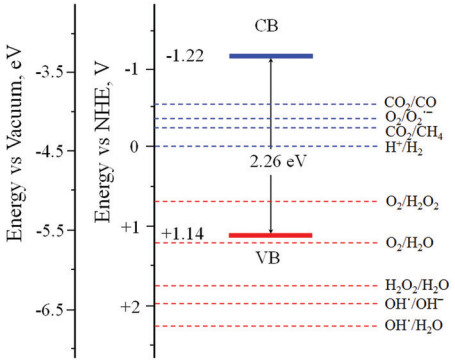

Fig. 8 Positions of the energy bands of the $BaBi_2O_4$-type barium bismuthate, $Ba_{1.264(4)}Bi_{1.971(4)}O_4$, with respect to a vacuum and with the electrochemical NHE scale. The positions of the top of the valence band (VB) and the bottom of the conduction band (CB) are manifested by solid red and blue lines, respectively. Dashed lines denote some electrochemical potentials of some important oxidation (red) and reduction (blue) half-reactions.

orbitals, while the conduction band is a mixture of bismuth and oxygen orbitals (see Fig. 7b). Fig. 7c illustrates the calculated optical absorption spectrum of the barium bismuthate; the lower-energy indirect transition is seen as being less intense than the higher-energy direct transition. Both peaks appear to be blue-shifted by $\sim$0.2 eV relative to the corresponding energies of the electronic transitions displayed in Fig. 7a.

Usage of the energy for the valence band (E_{VB} = +1.14 eV *vs.* NHE) and the bandgap energy E_g (2.26 eV) made it possible to determine the energy of the bottom of the conduction band: $E_{CB} = -1.22$ eV. The relevant band structure of the $BaBi_2O_4$-type bismuthate is presented in Fig. 8, together with the redox potentials of some important half-reactions.

2.3. Photoactivity of the $Ba_{1.264(4)}Bi_{1.971(4)}O_4$ bismuthate toward CO_2 reduction

The relative arrangement of energy bands and half-reaction potentials displayed in Fig. 8 suggest that the bismuthate is a suitable material for carrying out the reduction of carbon dioxide and the formation of superoxide radical anions. The potentials of most oxidation reactions (production of oxygen or hydrogen peroxide from water, and/or formation of $^{\bullet}$OH radicals) lie below the top of the valence band of the $Ba_{1.264(4)}Bi_{1.971(4)}O_4$ bismuthate so that these reactions are not expected to occur. However, under acidic conditions and in the presence of oxygen, reverse reactions may occur that might lead to corrosion of the bismuthate. Accordingly, confirmation of such an inference was obtained by carrying out the photoreduction of CO_2, chosen to explore the photocatalytic activity of the as-synthesized barium bismuthate sample, assessed photoelectrochemically in aqueous media in the PEC cell, and spectroscopically by IR techniques in the gas phase using an IR cell reactor.

The PEC cell used in the photoelectrochemical experiment consisted of two-compartment cathode–anode tandem system comprised of the ($Ba_{1.264(4)}Bi_{1.971(4)}O_4$/Ag)–($TiO_2$/FTO) tandem where $Ba_{1.264(4)}Bi_{1.971(4)}O_4$/Ag was the photocathode and TiO_2/FTO was the photoanode. The preparation of the electrodes and

Published on 04 February 2020. Downloaded by Lomonosov Moscow State University on 3/19/2020 4:47:56 PM.

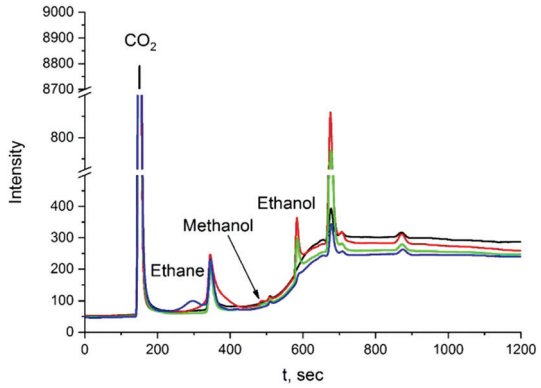

Fig. 9 Chromatograms of liquid samples from the cathode compartment of the PEC cell before and during the photoelectrochemical reaction: before irradiation (black) and after 1 h of irradiation (red), green after 2 h, and blue after 4 h.

the experimental details have been described elsewhere (see Experimental and Fig. S6 in ESI†). The photocathode compartment was filled with an oxygen-free $KHCO_3$ aqueous solution, while the photoanode compartment contained an $(NH_4)_2C_2O_4$ aqueous solution.

The successful course of the photoreduction of CO_2 in the photoelectrochemical cell was observed both visually and then confirmed by chromatographic analysis. Gas evolution was seen both in the photocathode and in the photoanode compartments of the photoelectrochemical cell. Relevant chromatograms of the liquid samples collected from the photocathode compartment before and during the photoprocess are illustrated in Fig. 9.

The principal changes in the chromatograms occur in the retention time regions of 300, 500 and 600 s. Additional detailed chromatograms covering these time intervals are also reported in Fig. S4 (ESI†). The reaction products were identified using predefined retention times of various substances that were suspected as possible products (Fig. S5, ESI†). During the search procedure for the products, the confidence interval of the occurrence of the chromatographic peaks of the tested possible products could be superimposed on the analyzed experimental peaks.

The results of chromatographic analyses showed that methanol and ethanol were the principal products that appeared after the first 2 h of irradiation of the photocathode compartment (Fig. S6, ESI†). Over the subsequent 2 h of irradiation, the quantity of these two products decreased significantly, while ethane formed and increased at the same time. The concentrations of the reaction products (Table 4) were determined using calibration curves of the tested substrates.

Based on the results of the chromatographic analyses, a tentative mechanism of the photoprocesses occurring in such a tandem system can thus be described; it is schematically illustrated in Fig. 10. When the photocathode and photoanode are both irradiated with light from a xenon lamp, photoexcitation of the barium bismuthate and the titanium dioxide led to the generation of electron/hole pairs. The photoelectrons at the photocathode participate in the photoreduction of carbon dioxide (present on the photocathode surface as carbonate ions)

Table 4 Concentrations of the main reaction products from the photocathode compartment of the photoelectrochemical cell

	Concentration of reduction products, mM		
Irradiation time, h	Methanol	Ethanol	Ethane
0	0	0	0
1	0.67	3.86	0
2	0.47	2.63	0
4	0.035	0.38	2.64

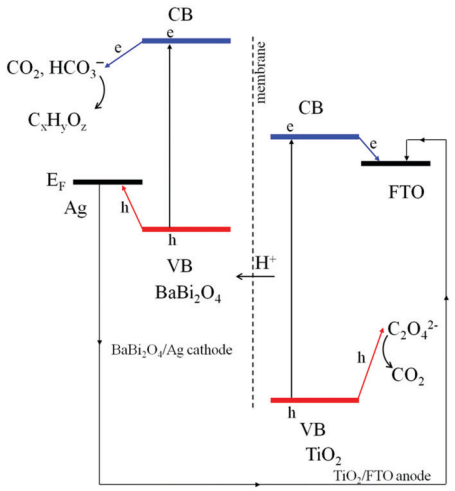

Fig. 10 Proposed scheme of the processes occurring in the photoelectrochemical cell in the $Ba_{1.264(4)}Bi_{1.971(4)}O_4$/Ag photocathode compartment and in the TiO_2/FTO photoanode compartment.

to alcohols and hydrocarbons, while the photoholes at the photoanode compartment are mainly spent in the oxidation of oxalate ions with formation of carbon dioxide. The membrane separating the two compartments of the PEC cell is permeable to migration of protons into the photocathode compartment, so that released protons are consumed in the reductive half-reactions. In turn, the photoholes accumulated on the silver substrate of the photocathode recombine with the photoelectrons on the FTO substrate of the photoanode. The initial photocurrent was 450 μA, which dropped to 300 μA throughout the photoreaction.

In order to exclude the possibility that the contact of the HCO_3^--containing electrolyte with the silver in the photocathode compartment might lead to the possible photoreduction of carbon dioxide, a blank experiment was carried out under otherwise identical experimental conditions in the (Ag)–(TiO_2/FTO) tandem system but without the barium bismuthate, where Ag and TiO_2/FTO were the photocathode and photoanode, respectively. No products were detected by gas chromatography in the liquid samples collected from the photocathode compartment of the PEC cell after irradiation of the system for 5 h.

The photoreduction of CO_2 gas in the gas/solid system was also carried out in the IR cell. Prior to the gas-phase experiment, the sample was thermally treated at 350 °C to reduce the amount of physisorbed water molecules and chemisorbed carbon dioxide species on the bismuthate's surface. Nonetheless, even after such

 This journal is © The Royal Society of Chemistry 2020

Published on 04 February 2020. Downloaded by Lomonosov Moscow State University on 3/19/2020 4:47:56 PM.

treatment, the sample surface remained highly hydrated and carbonated.

After introduction of CO_2 gas (10 Torr in equilibrium) into the IR cell reactor, the sample was irradiated by the Xe lamp at ambient temperature. The IR spectrum of such a treated barium bismuthate sample (Fig. S3, ESI,† spectrum 3) revealed broad absorption of molecular water at 3600–2700 cm^{-1}. The intense absorption with two maxima at 1363 cm^{-1} and 1442 cm^{-1} is caused by the C═O stretching vibrations of surficial carbonates,[34,35] the presence of which was also detected by XPS spectroscopy. This can be explained by the high affinity of carbon dioxide molecules for the surface of metal oxides containing alkaline-earth metal ions.

Difference IR spectra of barium bismuthate after irradiating the sample for 30 min (spectrum 1), and 100 min (spectrum 2) are also displayed in Fig. S3 (ESI†). Irradiation led to the removal of carbonates and water molecules adsorbed on the surface. In addition, the spectral feature at *ca.* 1442 cm^{-1} related to the carbonates (CO_3^{2-}) decreased in intensity, while the absorption at higher (1700–1500 cm^{-1}) and lower (1300–1150 cm^{-1}) wavenumbers increased. These spectral regions are attributed to the bicarbonate C═O stretching vibrations of HCO_3^-,[34,35] which may be the result of bicarbonate formation during carbonate protonation. The IR band of the asymmetric vibration of physisorbed CO_2 near 2350 cm^{-1} grows slightly during irradiation; concomitantly, a very weak peak of adsorbed carbon monoxide (2148 cm^{-1}) appears. All these observed spectral changes are amplified with the irradiation time. However, the alterations in the spectral region of the C–H stretching vibration (3000–2800 cm^{-1}) differ during the photoprocess (Fig. 10): first, C–H stretching bands appear after 30 min of irradiation (spectrum 1), followed by their disappearance after a longer irradiation time (spectrum 2), likely due to the formation of new CH-containing reaction products (probably hydrocarbons) that readily desorb owing to weak binding to the surface.

Evidently, some of the products formed are weakly adsorbed on the surface and so are mainly released and detected in the gas phase. Accordingly, it was imperative to examine the hydrophilicity of the surface of the barium bismuthate photocatalyst and possible photoinduced changes to the surface energy behavior during the heterogeneous photoreaction.

The initial hydrophilic state of the barium bismuthate was characterized by the water contact angle technique (WCA); initially the WCA was 35.0 ± 0.5 degrees. WCAs less than 40 degrees are typical of high-energy surfaces in air, as occurs on a metal-oxide surface. Note that IR and XPS spectroscopic results of the surface composition indicated the presence of strongly bound surface water and carbonate species. Undoubtedly, the presence of such surface species may reduce the WCA, and consequently the surface free energy (SFE).

The mean WCA for the irradiated bismuthate surface decreased to 26.0 ± 0.5 degrees subsequent to irradiation of the bismuthate sample for 2 h, which infers that band-to-band photoexcitation of the barium bismuthate leads to an increase of surface hydrophilicity (decrease in WCA) and hence to an increase of surface free energy. Recall that the IR spectra of the sample showed that upon irradiation the physisorbed water molecules and carbonate species are removed from the surface, and thus contribute to the increase in SFE. Evidently, adsorption of substances having polar groups and high surface tension (*e.g.*, water[36]) reduces the excess surface energy, and thus facilitates the supply of polar reagent molecules during the photoreduction of CO_2 in the liquid and gaseous phases, and the displacement of less polar molecules (*e.g.*, reaction products such as alkanes) from the surface as observed when carrying out the photoreduction of CO_2 on the barium bismuthate surface. Such occurrences are of great practical importance for solving the problem of isolating reaction products from the reaction mixture, especially when carrying out liquid-phase photocatalytic processes.

Summarizing all the experimental data presented above suggests additional details of the mechanism of the photocatalytic reduction of carbon dioxide on the surface of the $Ba_{1.264(4)}Bi_{1.971(4)}O_4$ photocatalyst in the IR cell. At first, carbon dioxide molecules from the gas phase are readily adsorbed on the surface, mostly in the form of carbonate functions (Fig. S3, ESI†). Photoexcitation of the sample in its intrinsic absorption region then leads to the formation of electron/hole photocarrier pairs (Fig. 8). Photoelectrons are subsequently consumed (Fig. 10) by the photoreduction of surface carbonates with formation of such products as carbon monoxide and hydrocarbons. Owing to the photoinduced increase in surface free energy (increased hydrophilicity of the surface), the non-polar alkanes formed are then easily removed from the surface of the barium bismuthate.

Although experimental results on the photoelectrochemical reduction of CO_2 over the $Ba_{1.264(4)}Bi_{1.971(4)}O_4$ surface obtained in the liquid phase and in the gaseous phase reactions show some differences in the nature of the reaction products, they do share some common events. Moreover, the results confirm the relative location of the energy bands of the barium bismuthate $Ba_{1.264(4)}Bi_{1.971(4)}O_4$ with respect to the redox potentials of the half-reactions, implicating reduction of CO_2 (Fig. 8).

As an additional test to assess the activity (or lack thereof) of the barium bismuthate, the photodegradation of phenol was also investigated in an aqueous suspension of the as-synthesized metal-oxide photocatalyst sample in a batch-type reactor, as phenol is often used as an ideal substrate to examine the photoactivity of potential metal-oxide photocatalysts. The time course of the concentration of phenol in the aqueous suspension under irradiation for more than 6 h is displayed in Fig. S7 (ESI†). Within experimental error, the $Ba_{1.264(4)}Bi_{1.971(4)}O_4$ bismuthate had no effect on the oxidative decomposition of phenol when photoexcited in its intrinsic absorption region (*ca.* 550 nm) in the batch reactor with light at $\lambda > 300$ nm.

3. Experimental

3.1. Synthesis and characterization of the barium bismuthate

The novel barium bismuthate was prepared *via* a solid-state synthesis. For this purpose, two precursors, barium nitrate $BaNO_3$ (≥99.5% purity; ACROS Chemicals) and bismuth(III)

Published on 04 February 2020. Downloaded by Lomonosov Moscow State University on 3/19/2020 4:47:56 PM.

oxide (Bi_2O_3, ≥99.5% purity; ACROS Chemicals) were mixed in a ratio corresponding to 15.0 mol% on a phase diagram. The mixture was then carefully ground in an agate mortar for 10 min in the presence of absolute ethanol (purity ≥ 99.8% (GC), Vekton). The mixture was subsequently heated in two stages: during the first stage, barium nitrate was converted to barium oxide on heating at 650 °C for 12 h in air; in the second stage, formation of the single-phase barium bismuthate was achieved upon heating at 750 °C for at least 72 h also in air, followed by intermediate grinding and pressing of the reaction mixture every 10–12 h. More detailed stages of the formation of the barium bismuthate are given in the ESI,† and the corresponding text.

The phase composition of the bismuthate was examined by X-ray diffraction (XRD) and by Raman spectroscopy. Powder diffraction data of $Ba_xBi_yO_{(2x+3y)/2}$ were collected at ambient temperature using a Bruker D8 ADVANCE powder diffractometer with CuKα radiation and a linear VANTEC detector, following which the data were refined by the Rietveld method. The 2θ data collection interval was 0.016 degrees and the collection time was 1 s. Rietveld refinement was performed using the program TOPAS 4.2.[37] Raman spectra were recorded in the 80–1525 cm^{-1} spectral region at ambient temperature using a SENTERRA Raman spectrophotometer (Bruker; resolution, 2 cm^{-1}; laser excitation wavelength, 785 nm; laser beam power, 1 mW).

The morphology of the sample was determined by scanning electron microscopy (SEM; TESCAN, Czech Republic; acceleration voltage, 20 kV). The elemental composition and its distribution in the as-synthesized barium bismuthate sample were established by energy dispersive X-ray spectroscopy (EDX; X-Max^N, Oxford Instruments, UK). The specific surface area of the sample pretreated at 350 °C for 6 h was determined by the BET method using a Quadrasorb SI surface area analyzer (N_2 adsorption).

The elemental composition of the surface and the position of the valence band (VB) were determined by X-ray photoelectron spectroscopy (XPS) using a Thermo Fisher Scientific Escalab 250Xi spectrophotometer (Al Kα radiation, 1486.6 eV; spectral resolution, 0.5 eV); the reference carbon line C1s of a C–C bond was taken at a binding energy (BE) of 284.8 eV.[38]

Diffuse reflectance spectra, as $R(\lambda)$, were recorded in the 375–775 nm spectral range under ambient conditions on a Cary 5000 UV/vis/NIR spectrophotometer equipped with a DRA 2500 external diffuse reflectance accessory; optical grade $BaSO_4$ powder was the reference standard.

The hydrophilic properties of barium bismuthate were ascertained in the dark and under irradiation. The powdered sample was pressed into a self-supported pellet with dimensions 40/40/2 mm (width/height/thickness) using a hydraulic press. The surface hydrophilicity was characterized by determining the water contact angles (WCA) using a Theta Lite optical tensiometer (Biolin Scientific, Finland). To obtain greater reproducibility, the water contact angles were measured no less than six times after each manipulation; the average WCA value is reported. The photoinduced surface hydrophilicity of the barium bismuthate sample was ascertained by irradiating with light of various spectral compositions under stationary ambient conditions (temperature: +20 °C, relative humidity: *ca.* 50%). For this purpose, a 150 W xenon lamp (OSRAM, light irradiance, 7.3 mW cm^{-2}) was used; the total exposure time was 2 h.

3.2. Photoactivity of the $BaBi_2O_4$-type bismuthate

3.2.1. Photoelectrochemical CO_2 reduction from aqueous solutions. The photocatalytic activity of the as-synthesized barium bismuthate was evaluated *via* the photoelectrochemical reduction of CO_2, which was carried out in a 100 mL, two compartment photoelectrochemical (PEC) cell used in the wired configuration with anatase TiO_2 as the photoanode and barium bismuthate as the photocathode separated by a proton-permeable membrane (DuPont™ Nafion® N-424). The electrical connection between the photoanode and photocathode was established by a copper wire. Both electrodes were irradiated with light from the 150 W xenon lamp; the applied potential between the electrodes was 100 mV. A schematic of the photoelectrochemical (PEC) cell is illustrated in Fig. S6 (ESI†).

Photoreduction of CO_2 occurred in the photocathode compartment enclosed by a quartz window. The compartment was first filled with a 0.5 M $KHCO_3$ aqueous solution, followed by purging the solution with gaseous carbon dioxide for 1 h to saturate the solution with CO_2 and to remove oxygen from the electrolyte prior to irradiation. The photoanode compartment was also enclosed by a quartz window. Photooxidation of ammonium oxalate, $(NH_4)_2C_2O_4$, was chosen as the counter reaction occurring in the photoanode compartment; the electrolyte consisted of an equimolar aqueous solution of 0.2 M K_2SO_4 and 0.2 M $(NH_4)_2C_2O_4$.

Preparation of the photocathode with the as-synthesized barium bismuthate consisted of compressing the powder using a hydraulic press into a pellet with dimensions of 21/31/2 mm (width/height/thickness). A silver-based conductive paste was applied to one side of this pellet, following which a copper wire was soldered to it and then coated with epoxy for electrical insulation. The photocathode so prepared provided only contact between the barium bismuthate pellet and the electrolyte.

The photoanode consisted of a thin film of anatase TiO_2 deposited on FTO glass (25 × 25 mm, industrial glass; sheet resistance, $<100\ \Omega\ sq^{-1}$) using a sol–gel method and a two-step dip-coating technique (KSV Nima dip coater). The TiO_2 sol was prepared by mixing titanium isopropoxide (9 mL, 97%, Sigma Aldrich), isopropyl alcohol (100 mL, ≥99.0%, Vekton), and citric acid (18 g, chemical grade, Vekton) as the starting material, as the solvent, and as the stabilizer, respectively. In the first stage, a dense thin film was formed by 5-fold immersion at a withdrawal velocity of 10 mm min^{-1} with 5 min air drying between each immersion, after which the FTO substrate was immersed into the same sol at a withdrawal velocity of 50 mm min^{-1} five more times. Subsequently, the coating was annealed at 500 °C for 6 h in air at a heating/cooling rate of 1 deg min^{-1}. To further develop the electrode surface, a rough film was formed on top of the dense film by 5-fold immersion at withdrawal velocities of 50 mm min^{-1} and 100 mm min^{-1} with heating to 200 °C in air between immersions. Finally, the coating was annealed at 500 °C for 6 h in air at a heating/cooling rate

 This journal is © The Royal Society of Chemistry 2020

Published on 04 February 2020. Downloaded by Lomonosov Moscow State University on 3/19/2020 4:47:56 PM.

of 1 deg min^{-1}. The uncoated corner of the substrate was connected with a copper wire, which was isolated from the solution with sealing rings (Fig. S1, ESI†).

Liquid samples from the photocathode compartment of the PEC cell were analyzed chromatographically using a Chromatec Crystal 5000 gas chromatograph equipped with a 3 m × 2 mm HayeSep R 80/100 column and a methanator; helium was the carrier gas. The gas flow rate was 25 mL min^{-1}. The temperatures of the evaporator, methanator, and flame-ionization detector were 200 °C, 325 °C, and 200 °C, respectively. The temperature of the starting column (40 °C) was increased to 200 °C at a heating rate of 20 degrees min^{-1}. Before analyzing the reaction probes, chromatograms of some known alcohols and hydrocarbons were obtained to determine possible reaction products (Fig. S2, ESI†). The retention times of these products from the chromatographic column were determined under otherwise identical experimental conditions. Calibration curves for all the substances tested were used to determine the respective concentrations of products.

3.2.2. FTIR spectroscopic study of photoreduction of CO_2 in the gas phase. The stainless-steel cell used to examine the infrared spectra of the adsorbed species in transmission mode was also used in carrying out the spectroscopic study of the photocatalytic reduction of CO_2 gas over barium bismuthate. The cell's construction and operating mode have been described in detail elsewhere by Bulanin and coworkers.[39]

Prior to the photoinduction experiment, a powdered barium bismuthate sample was pressed into a thin self-supported pellet (thickness, 0.1 mm; specific weight, 9.4 g cm^{-3}), which was then annealed at 350 °C (620 K) in a vacuum (10^{-4} Torr) for 2 h and then in oxygen for 2 h followed by cooling to ambient temperature and thorough evacuation of the sample. Subsequently, gaseous carbon dioxide (10 Torr in equilibrium) was introduced onto the barium bismuthate sample at ambient temperature, followed by irradiating the sample with a 150 W xenon lamp (irradiance, 7.3 mW cm^{-2}) for 100 min.

During the experiment, IR spectra of the sample and of the gas phase in the sample-containing volume were recorded in the 1000–3800 cm^{-1} spectral region at ambient temperature using a Thermo Scientific Nicolet iS50 FTIR spectrophotometer equipped with a DTGS detector; between 600 and 2000 scans were collected to obtain the IR spectra at a spectral resolution of 6 cm^{-1}.

3.2.3. Liquid-phase photodegradation of phenol. To assess the photocatalytic visible-light-activity (or lack thereof) of the bismuthate sample we used the photodecomposition of phenol in an aqueous suspension in a batch-type reactor equipped with a quartz window for UV irradiation under ambient conditions. Before irradiation, the aqueous suspension (photocatalyst loading, 1.0 g L^{-1}; pH, 7.0; volume, 300 mL) was treated in an ultrasonic processor for 10 min followed by addition of 100 ppm of phenol (Aldrich; purity, 99.5%; 1.06 mM) and then magnetically stirred for 1 h under dark conditions to achieve an adsorption–desorption equilibrium. The selected initial concentration of phenol ensured that the reaction rate was independent of concentration. The light source was a 150 W xenon lamp (OSRAM); an optical cutoff filter removed UV wavelengths below 300 nm (light irradiance, 7 mW cm^{-2}) so as to prevent direct photolysis of phenol through light absorption by the substrate.

To determine the time course of the concentration of phenol, aliquot samples were collected at given intervals and then analyzed by HPLC analysis performed using a 1260 Infinity liquid chromatograph equipped with a UV/vis detector and a C18 column (Agilent Technologies). Prior to the chromatographic analysis, samples were filtered through a 0.2 μm Minisart filter to remove any solid particles. The mobile phase was a 50/50 v/v mixture of methanol/water; the detection wavelength was 210 nm and the bandwidth was 4 nm.

The initial rate of the photocatalytic reaction, often taken as characteristic of the activity of a photocatalyst, in the present case the as-synthesized barium bismuthate, was determined from the kinetic approximation:

$$C(t) = C_0 \exp(-kt) \quad (2)$$

so that

$$dC/dt_{(t\to 0)} = kC_0 \quad (3)$$

where k is the apparent quasi-first-order rate constant.

4. Computational specifics

Periodic DFT calculations were performed using the GGA Perdew–Burke–Ernzerhof (PBE) density functional[40,41] as implemented in the ABINIT 6.8.3 program.[42] A basis set in the form of the Troullier–Martins norm-conserving pseudopotentials[43] was employed with a kinetic energy cutoff of 30 Hartree. The $R\bar{3}m$ symmetry of the material's crystal lattice determined from the XRD analysis was enforced in all calculations. The Brillouin zone (BZ) was sampled over the automatically generated Γ-point-centered 8 × 8 × 8 Monkhorst–Pack grid of k-points.[44] The electronic band structure was computed at 81 k-points along the Γ–F–L–$L1$–Z high symmetry path of the trigonal BZ. The default total energy convergence criterion of 1.0×10^{-8} Hartree was applied. The electronic band structure and density of states were plotted using the Gnuplot 5.2 software package.[45] Optical absorption spectra were computed based on the Bethe–Salpeter equation.[46]

5. Concluding remarks

This study reports on the synthesis and comprehensive characterization of a most promising semiconductor photocatalyst of the $BaBi_2O_4$ class, which following Rietveld refinement can be described as $Ba_{1.264(4)}Bi_{1.971(4)}O_4$. Various experimental techniques (XPS, DRS, SEM, and EDX) were brought to bear on its characterization, and together with a computational approach (DFT) the relevant energy band structure of this novel material was determined. The energies of the valence band and the conduction band were +1.14 eV and −1.12 eV, respectively; the indirect bandgap of this bismuthate semiconductor was E_g = 2.26 eV (absorption edge ≈ 550 nm). Accordingly, this bismuthate system is a potentially viable visible-light-active

Published on 04 February 2020. Downloaded by Lomonosov Moscow State University on 3/19/2020 4:47:56 PM.

photocatalyst. Both energies are rather high in comparison to those for most known photocatalysts. However, such an anomalous energy arrangement of the conduction band opens up unique possibilities for using this bismuthate for the photocatalytic reduction of a currently controversial greenhouse gas, carbon dioxide, while oxidative half-reactions appear rather unlikely as attested by the lack of photoinduced oxidation of phenol. The photoreduction of CO_2 over the $Ba_{1.264(4)}Bi_{1.971(4)}O_4$ surface was examined photoelectrochemically in a PEC cell in aqueous media and spectroscopically using an IR cell reactor for the photoreduction in the gas phase. Chromatographic analyses of the reaction products revealed that the main products differed somewhat: a mixture of carbon monoxide and alkanes from adsorbed CO_2 in the gas/solid system *versus* a mixture of alcohols and alkanes from the liquid/solid system. No attempts were made in the present study to optimize the experimental conditions.

Conflicts of interest

There are no conflicts to declare.

Acknowledgements

The current research was kindly funded by a grant from the Russian Science Foundation (project No. 19-73-10013). R. K., A. V. R., V. K. R. and T. V. B. acknowledge financial support from Saint-Petersburg State University (Pure ID 39054581). A. V. R. thanks the Russian Foundation for Basic Research for a Grant No. 18-03-00855 that supported studies into the photoinduced hydrophilicity of the bismuthate. The authors are further grateful to the staff of the Khabarovsk Innovation and Analytical Center of the Yu. A. Kosygin Institute of Tectonics and Geophysics of the Far Eastern Branch of the Russian Academy of Sciences, and the Resource Centers of the Research Park at the Saint-Petersburg State University: (i) the Center for Diagnostics of Functional Materials for Medicine, Pharmacology and Nanoelectronics, (ii) the Center for Physical Methods of Surface Investigation, (iii) the Center for Optical and Laser Materials Research, and the laboratories of (iv) Nanotechnology and (v) Nanophotonics for their valuable assistance in carrying out the research and in providing the needed equipment. One of us (N.S.) is grateful to Prof. Angelo Albini and the staff of the PhotoGreen Laboratory at the University of Pavia, Italy, for their continued hospitality.

Notes and references

1 L. V. Bora and R. K. Mewada, *Renewable Sustainable Energy Rev.*, 2017, **76**, 1393–1421.
2 X. Wang, F. Wang, Y. Sang and H. Liu, *Adv. Energy Mater.*, 2017, **7**, 1700473.
3 T. Tatarchuk, A. Peter, B. Al-Najar, J. Vijaya and M. Bououdina, in *Nanotechnology in Environmental Science*, ed. C. M. Hussain and A. K. Mishra, Wiley-VCH Verlag GmbH & Co. KGaA, Weinheim, Germany, 2018, ch. 8, pp. 209–292.
4 X. Li, J. Yu, M. Jaroniec and X. Chen, *Chem. Rev.*, 2019, **119**, 3962–4179.
5 D. S. Shtarev, A. V. Shtareva, V. K. Ryabchuk, A. V. Rudakova, P. D. Murzin, M. S. Molokeev, A. V. Koroleva, A. I. Blokh and N. Serpone, *Catal. Today*, 2020, **340**, 70–85.
6 D. S. Shtarev, A. I. Blokh, E. O. Nashchochin and A. V. Shtareva, *Opt. Quantum Electron.*, 2018, **50**, 228.
7 D. S. Shtarev, A. V. Shtareva, V. K. Ryabchuk, A. V. Rudakova and N. Serpone, *ChemCatChem*, 2019, **11**, 3534–3541.
8 Y. C. Yang, X. Z. Wang and J. Qu, *Appl. Mech. Mater.*, 2014, **522–524**, 411–415.
9 W. Zhou and X. Yu, *Desalin. Water Treat.*, 2011, **30**, 295–299.
10 Z. Shan, Y. Xia, Y. Yang, H. Ding and F. Huang, *Mater. Lett.*, 2009, **63**, 75–77.
11 Y. Obukuro, S. Matsushima, K. Obata, T. Suzuki, M. Arai, E. Asato, Y. Okuyama, N. Matsunaga and G. Sakai, *J. Alloys Compd.*, 2016, **658**, 139–146.
12 X. Hu, C. Hu and J. Qu, *Appl. Catal., B*, 2006, **69**, 17–23.
13 C. Hu, X. Hu, J. Guo and J. Qu, *Environ. Sci. Technol.*, 2006, **40**, 5508–5513.
14 S.-H. Lee, W.-H. Jung, J.-H. Sohn, J.-H. Lee and S.-H. Cho, *J. Appl. Phys.*, 1999, **86**, 6351–6354.
15 J. Tang, Z. Zou and J. Ye, *J. Phys. Chem. C*, 2007, **111**, 12779–12785.
16 T. Hatakeyama, S. Takeda, F. Ishikawa, A. Ohmura, A. Nakayama, Y. Yamada, A. Matsushita and J. Yea, *J. Ceram. Soc. Jpn.*, 2010, **118**, 91–95.
17 M. Khraisheh, A. Khazndar and M. A. Al-Ghouti, *Int. J. Energy Res.*, 2015, **39**, 1142–1152.
18 J. Ge, W.-J. Yin and Y. Yan, *Chem. Mater.*, 2018, **30**, 1017–1031.
19 B. Yan, M. Jansen and C. Felser, *Nat. Phys.*, 2013, **9**, 709–711.
20 N. C. Plumb, D. J. Gawryluk, Y. Wang, Z. Ristic, J. Park, B. Q. Lv, Z. Wang, C. E. Matt, N. Xu, T. Shang, K. Conder, J. Mesot, S. Johnston, M. Shi and M. Radović, *Phys. Rev. Lett.*, 2016, **117**, 037002.
21 B. Weng, Z. Xiao, W. Meng, C. R. Grice, T. Poudel, X. Deng and Y. Yan, *Adv. Energy Mater.*, 2017, **7**, 1602260.
22 Y.-Y. Wang, G. F. Feng, T. E. Sutto and Z. Shao, *Phys. Rev. B: Condens. Matter Mater. Phys.*, 1991, **44**, 7098–7101.
23 H. Namatame, A. Fujimori, H. Takagi, S. Uchida, F. M. F. de Groot and J. C. Fuggle, *Phys. Rev. B: Condens. Matter Mater. Phys.*, 1993, **48**, 16917–16925.
24 S. N. Habisreutinger, L. Schmidt-Mende and J. K. Stolarczyk, *Angew. Chem., Int. Ed.*, 2013, **52**, 7372–7408.
25 Y. Matsumoto, *J. Solid State Chem.*, 1996, **126**, 227–234.
26 P. Conflant, J. C. Boivin, G. Nowogrocki and D. Thomas, *Solid State Ionics*, 1983, **9–10**(Part 2), 925–928.
27 CCDC 1962724†.
28 V. N. Denisov, A. N. Ivlev, A. S. Lipin, B. N. Mavrin and V. G. Orlov, *J. Phys.: Condens. Matter*, 1999, **23**, 4967–4978.
29 D. de Waal, K.-J. Range, M. Konigstein and W. Kiefer, *J. Raman Spectrosc.*, 1998, **29**, 109–113.
30 W. Luo, J. Tang, Z. Zou and J. Ye, *J. Alloys Compd.*, 2008, **455**, 346–352.

 This journal is © The Royal Society of Chemistry 2020

Published on 04 February 2020. Downloaded by Lomonosov Moscow State University on 3/19/2020 4:47:56 PM.

31 R. J. Betsch and W. B. White, *Spectrochim. Acta, Part A*, 1978, **34**, 505–514.
32 F. D. Hardcastle and I. E. Wachs, *J. Solid State Chem.*, 1992, **97**, 319–331.
33 S. A. Chambers, T. Droubay, T. C. Kaspar, M. Gutowski and M. van Schilfgaarde, *Surf. Sci.*, 2004, **554**, 81–89.
34 F. A. Miller and C. H. Wilkins, *Anal. Chem.*, 1952, **24**, 1253–1294.
35 G. Socrates, *Infrared and Raman characteristic group frequencies. Tables and Charts*, John Wiley & Sons, Chichester, UK, 2001.
36 Dortmund Data Bank; see http://www.ddbst.com/, accessed October 2019.
37 Bruker AXS TOPAS V4: General profile and structure analysis software for powder diffraction data. – User's Manual, Bruker AXS, Karlsruhe, Germany, 2008.
38 NIST X-ray Photoelectron Spectroscopy Database; see https://www.srdata.nist.gov/xps/, accessed October 2019.
39 K. M. Bulanin, D. W. Bahnemann and A. V. Rudakova, *Rev. Sci. Instrum.*, 2019, **90**, 105113.
40 J. P. Perdew, K. Burke and M. Ernzerhof, *Phys. Rev. Lett.*, 1996, **77**, 3865–3868.
41 J. P. Perdew, K. Burke and M. Ernzerhof, *Phys. Rev. Lett.*, 1997, **78**, 1396.
42 X. Gonze, B. Amadon, P. M. Anglade, J.-M. Beuken, F. Bottin, P. Boulanger, F. Bruneval, D. Caliste, R. Caracas, M. Cote, T. Deutsch, L. Genovese, Ph. Ghosez, M. Giantomassi, S. Goedecker, D. Hamann, P. Hermet, F. Jollet, G. Jomard, S. Leroux, M. Mancini, S. Mazevet, M. J. T. Oliveira, G. Onida, Y. Pouillon, T. Rangel, G.-M. Rignanese, D. Sangalli, R. Shaltaf, M. Torrent, M. J. Verstraete, G. Zérah and J. W. Zwanziger, *Comput. Phys. Commun.*, 2009, **180**, 2582–2615.
43 N. Troullier and J. L. Martins, *Phys. Rev. B: Condens. Matter Mater. Phys.*, 1991, **43**, 1993.
44 H. J. Monkhorst and J. D. Pack, *Phys. Rev. B: Solid State*, 1976, **13**, 5188–5192.
45 T. Williams, C. Kelley, E. A. Merritt, C. Bersch, H.-B. Bröker, J. Campbell, R. Cunningham, D. Denholm, G. Elber, R. Fearick, C. Grammes, L. Hart, L. Hecking, P. Juhász, T. Koenig, D. Kotz, E. Kubaitis, R. Lang, T. Lecomte, A. Lehmann, J. Lodewyck, A. Mai, B. Märkisch, P. Mikulík, D. Sebald, C. Steger, S. Takeno, T. Tkacik, J. van der Woude, J. R. van Zandt, A. Woo and J. Zellner, *Gnuplot 5.2: An interactive plotting program*, 2018; see http://www.gnuplot.info/docs_5.2/Gnuplot_5.2.pdf, accessed November 2019.
46 E. E. Salpeter and H. A. Bethe, *Phys. Rev.*, 1951, **84**, 1232–1242.